ADVANCED MATERIALS
www.advmat.de

www.MaterialsViews.com

Covalently Connected Carbon Nanostructures for Current Collectors in Both the Cathode and Anode of Li–S Batteries

Song Jin, Sen Xin, Linjun Wang, Zhenzhen Du, Lina Cao, Jiafeng Chen, Xianghua Kong, Ming Gong, Junling Lu, Yanwu Zhu, Hengxing Ji, and Rodney S. Ruoff*

The lithium–sulfur (Li–S) battery has a theoretical specific energy of 2600 W h kg^{-1} that is 3–5 times that of Li-ion batteries. However, in the cathode, the low electrical conductivity of sulfur (5×10^{-30} S cm^{-1}) and dissolution of polysulfides result in a poor specific power and fast capacity decay on cycling,[1–3] and in the anode the use of lithium metal foil leads to dendritic growth that raises serious safety issues,[4,5] which have long been identified as major issues for the development of Li–S batteries.[6–10] To overcome these issues, a variety of modifications has been considered, for example, tailoring the sulfur composite nanostructure,[11–13] modifying the separator surface,[14,15] and using innovative electrolytes and electrolyte additives such as $LiNO_3$.[16]

In the cathode, recent research has focused on filling porous discrete carbon nano/microparticles with sulfur in which the carbon acts as a transport medium for charge formed in the sulfur and prevents polysulfide dissolution because of its tunable pore structure.[12,17–20] Pioneering studies indicate ways to optimize the sulfur cathode, including the uniform distribution of sulfur in the carbon, fine control of the sulfur particle size to less than 10 nm, and a well-designed pore structure of the carbon. In the anode, on the other hand, focus has been on the lithium metal because sulfur has a low discharge potential (2.1 V vs Li/Li^+) compared to many other cathode materials,[1] therefore the use of lithium metal in the anode is critical to ensure a reasonable output voltage without energy loss for a Li–S battery. Unfortunately, the uncontrollable dendritic lithium growth during battery charge/discharge inherent in a Li–S battery causes safety hazards. This same issue has also hindered the use of lithium metal in rechargeable batteries over the past 40 years.[21,22] Most approaches to dendrite prevention focus on optimizing electrolytes to obtain a stable and uniform solid electrolyte interphase (SEI).[23,24] Recent studies found physical protective layers are effective in suppressing lithium dendrite formation.[25,26] These methods are based on the use of a strong mechanical barrier provided by the SEI or coating layers to prevent lithium dendrites penetrating the separator, yet do not affect lithium metal dendrite formation.

The current collector is a key component of both the cathode and anode and has a significant influence on the electrochemical performance of batteries. A conventional sulfur cathode is prepared by coating an aluminum foil, as current collector, with a slurry containing the S/C composite, a binder, and carbon black. If we take typical values of a 70 wt% sulfur in the composite and 80 wt% composite in the dried slurry that is coated on a 25 μm thick aluminum foil (density 2.7 g cm^{-3}) current collector with an area loading density of the sulfur of around 6 mg cm^{-2}, a rough calculation yields a 34 wt% sulfur content in the cathode. In the cathode the free electrons generated upon charging/discharging have to transfer from particle to particle until they reach the planar aluminum current collector, and interparticle boundaries are one of the major reasons for the poor electrode reaction kinetics at a high current density. In addition, the formation of a passive layer on and/or corrosion of the aluminum and other metal current collectors are related to the self-discharge of Li-ion batteries.[27] On the other hand, lithium dendrite nucleation on the planar foil is triggered by an inhomogeneous surface such as crystal steps, and dendrite growth is accelerated at high current densities as a result of a near zero Li^+ concentration at the foil surface and a greater electric field gradient at the dendrite tips.[28,29]

Here, we report a 3D current collector composed of hundreds of micrometer-long carbon nanotube bundles that are connected

S. Jin, Z. Z. Du, J. F. Chen, Prof. Y. W. Zhu, Prof. H. X. Ji
Department of Materials Science and Engineering
CAS Key Laboratory of Materials for Energy Conversion
iChEM (Collaborative Innovation Center of Chemistry for Energy Materials)
University of Science and Technology of China
Hefei 230026, China
E-mail: jihengx@ustc.edu.cn

Prof. S. Xin, Prof. X. H. Kong
School of Chemistry and Chemical Engineering
Hefei University of Technology
Hefei 230009, China

Dr. L. J. Wang
Hefei National Laboratory for Physical Sciences at the Microscale and Center for Micro- and Nanoscale Research and Fabrication
University of Science and Technology of China
Hefei 230026, China

L. N. Cao, Prof. J. L. Lu
Department of Chemical Physics and CAS Key Laboratory of Materials for Energy Conversion
University of Science and Technology of China
Hefei 230026, China

Prof. M. Gong
Material Test and Analysis Lab
Engineering and Materials Science Experiment Center
University of Science and Technology of China
Hefei 230026, China

Prof. R. S. Ruoff
Center for Multidimensional Carbon Materials (CMCM)
Institute for Basic Science (IBS) Center at the Ulsan National Institute of Science & Technology (UNIST) Campus
Department of Chemistry and School of Materials Science
UNIST
Ulsan 689-798, South Korea

DOI: 10.1002/adma.201602704

by covalent carbon–carbon bonds to an ultrathin graphite foam (CNT-UGF). When filling the CNT-UGF with elemental sulfur without any additional binder or carbon black, the cathode contains 43 wt% (areal loading density of 2.4 mg cm^{-2}) sulfur, delivers a capacity decay rate of 0.063% per cycle after 400 charge/discharge cycles at 0.5 C (1 C = 1675 mA h g^{-1} with respect to the mass of sulfur). When the CNT-UGF is electroplated with lithium metal, the anode cycles with a voltage hysteresis of 14% of that of the lithium foil for more than 800 h without short circuiting, although a short circuit occurs in a lithium foil anode after 260 h. A Li–S cell assembled with the S/CNT-UGF cathode (47 wt% sulfur content, areal loading density of 2.6 mg cm^{-2} of sulfur) and the Li/CNT-UGF anode (20 wt% lithium content) delivers a high-rate capacity of 860 mA h g^{-1} at 12 C, corresponding to a remarkable specific power of 8680 W kg^{-1} with a specific energy of 720 Wh kg^{-1} with respect to the mass of the cathode.

By finely tuning the CNT synthesis parameters (see Experimental Section and Figure S1 of the Supporting Information for details), we prepared a CNT-UGF hybrid by chemical vapor deposition (**Figure 1**a–c)[30–32] and obtained compact CNT bundles standing on the UGF struts with lengths in the range of tens to hundreds of micrometers (Figures 1d–g). When the CNT length reaches hundreds of micrometers, the original 400 µm large pores of the UGF are filled with CNT bundles and are invisible (Figures 1a,f). Raman spectroscopy shows a strong 2D peak (Figure 1h) and thermogravimetric analysis (TGA) shows a significant weight loss in air at temperatures higher than 580 °C (Figure 1i), indicating 94.3 wt% of sp^2-hybridized carbon in the hybrid. Nitrogen adsorption/desorption isotherms together with Brunauer–Emmett–Teller analysis show that the CNT-UGF hybrid has a specific surface area of ≈252 m^2 g^{-1}, pore volume of 1.08 cm^3 g^{-1} (Figure S2a,b,

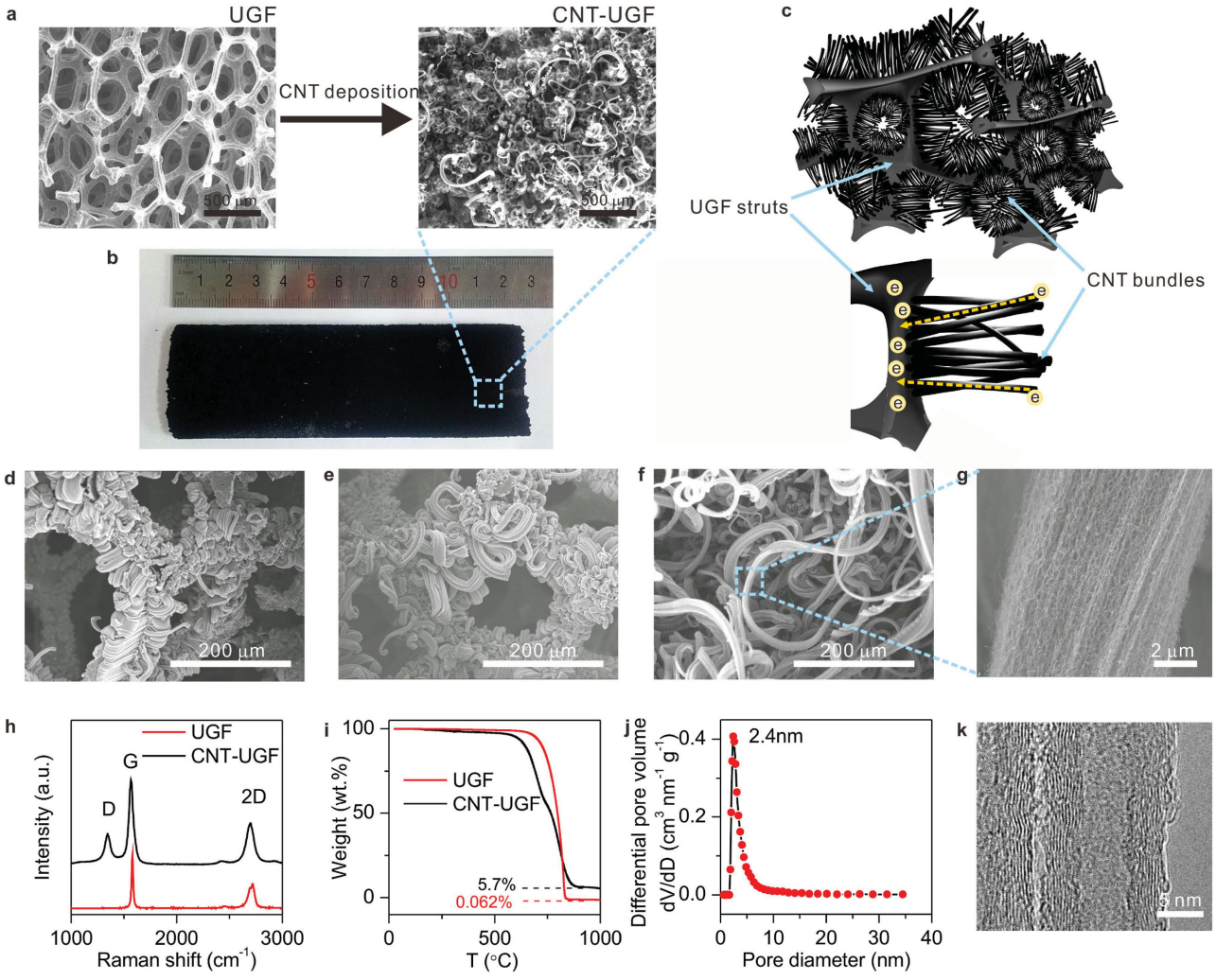

Figure 1. a) SEM images of UGF (left) and CNT-UGF hybrid (right). b) Photograph of a CNT-UGF hybrid with a geometric surface area of 50 cm^2. c) Schematic of the 3D interconnected network of the CNT-UGF hybrid which allows free electron transfer between the UGF and each CNT. d–f) SEM images of the CNT-UGF with different CNT lengths. g) SEM image of the CNT bundle marked by the blue dashed square in (f). h) Raman spectra of an as-grown CNT-UGF and UGF. The D peak in the Raman spectrum originates from defects in the CNTs, and does not exist in the spectrum of UGF. i) TGA curves of UGF and CNT-UGF hybrid. The 5.7 wt% residue obtained after heating the CNT-UGF hybrid in air at 1000 °C is from the Fe catalyst and Al_2O_3 buffer deposited for CNT growth. j) Pore size distribution of the CNT-UGF hybrid measured by N_2 adsorption/desorption isotherms and fitted by density functional theory. k) High resolution transmission electron microscopy (HRTEM) image of a CNT.

Supporting Information), and an average pore size of 2.4 nm (Figure 1j) which are very likely caused by the CNT bundles (Figure 1g,k). A sample of the hybrid material tens of square centimeters in area could be readily fabricated (Figure 1b), indicating its potential in scaled production and use. The measured mass density (without compressing) was around 12.4 mg cm^{-3} with a CNT content of around 73.9 wt% (Table S1, Supporting Information). In this structure, the CNT bundles provide (a) a much larger surface area than the UGF and (b) optimized nanometer-size pores to accommodate the electrochemically active materials such as sulfur and lithium.

CNTs grow with the assistance of catalysts which adhere to either the root or tip of the tubes.[33,34] In the latter case, the CNT has the chance to directly bond to the graphite surface by carbon–carbon bonds, which enable the coupling of π-electrons in CNT and UGF, thus favoring charge transfer between the electrochemically active materials (sulfur for the cathode and lithium for the anode in a Li–S battery) and the out circuit that is connected to the battery during the electrochemical reaction. In our study, an Fe catalyst was deposited on the UGF before the Al_2O_3 buffer layer and the continuous catalyst/buffer layer is visible on top of the closely packed CNT bundles of the CNT-UGF hybrid (Figure S3a,b, Supporting Information), which is different from the structure formed when the Fe catalyst is deposited on the UGF after the Al_2O_3 buffer (Figure S3c,d, Supporting Information). These results are in agreement with the "Odako" growth process in which the Al_2O_3 layer is detached from the substrate and supports the catalytic growth of CNT bundles.[35] A transmission electron microscopy (TEM) image of the CNT–graphite junction (**Figure 2**a,b) shows that the CNT seamlessly connects to the graphite substrate with uniform contrast. Though the crystal structure of the CNT and graphite substrate were partially damaged by the ion milling used for specimen preparation and some 2 nm nanoparticles were found that were introduced, dark particles of iron catalyst with a size similar to the diameter of the CNTs were not found at the junction. The absence of Fe catalyst at the CNT–graphite junction and the chemical composition of the 2 nm large nanoparticles (gallium and platinum) were verified by HAADF-TEM images and EDX elemental maps of the CNT–graphite junction (Figure S4, Supporting Information). Moreover, lattice fringes (marked by black arrows in Figure 2c) with a separation of 0.335 nm that start from the CNTs and extend to the graphite substrate are visible in the high resolution TEM (HRTEM) image. A lattice fringe branch (indicated by a dashed yellow line) at the bottom of a CNT, yet connecting to a graphite fringe is also found, indicating direct carbon–carbon bonding of the CNT to the graphite. In addition, the CNT-UGF hybrid with

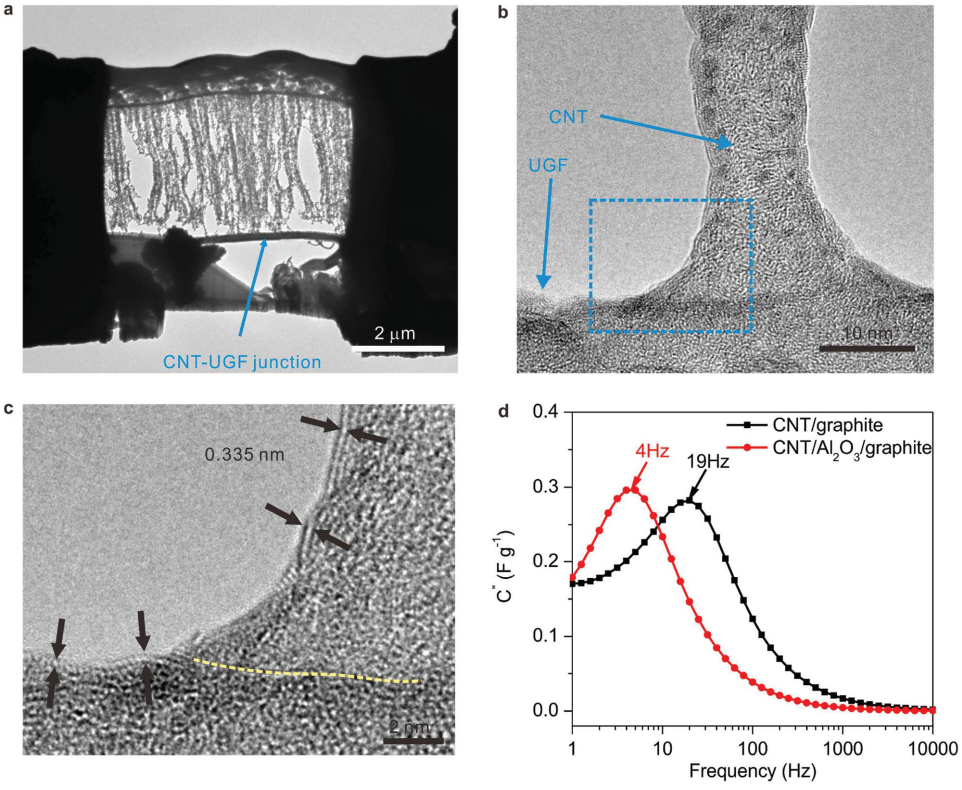

Figure 2. a) TEM image of a slice of the CNT-UGF hybrid prepared by focused ion beam (FIB) milling. b,c) High magnification TEM images of the CNT/graphite junction. The TEM image in (c) was acquired from the area marked by the blue dashed rectangle in (b). The black arrows in (c) denote fringe lines with a separation of 0.335 nm, and the yellow dashed line marks a fringe line under the CNT. d) Imaginary capacitance plotted against AC current frequency for the CNT-UGF hybrid with CNTs directly bonded to the graphite in which the catalyst layer was prepared by depositing Fe before an Al_2O_3 layer, and that for a CNT-UGF hybrid having an Al_2O_3 layer between the CNT and graphite (CNT/Al_2O_3/graphite) in which the catalyst layer was prepared by depositing Al_2O_3 before Fe. The peak frequency is the reciprocal of the time constant which is a measure of how fast the material can be charged/discharged.

the CNTs connected to the graphite with carbon bonds shows a five times faster charge transfer rate than that having Al_2O_3 between the CNTs and the graphite (Figure 2d). Because of the structural complexity and the low stability of the carbon during specimen preparation, it is still a challenge to determine the detailed structure of the CNT–graphite junctions at the atomic scale.

We loaded sulfur on the CNT-UGF (S/CNT-UGF cathode) by a simple melting-adsorption process (see Experimental Section of the Supporting Information for details), in which liquid S flowed and stored in the ultralong and continuous nanogaps of ≈2 nm in the CNT bundles via capillary action, yielding a maximum S content of ≈47 wt% in the whole cathode and corresponding to an areal loading density of 2.6 mg cm^{-2} per unit area of the electrode disc (**Figure 3**a,b, Figure S5a, Supporting Information). The density of the S/CNT-UGF electrodes after being compressed by the coin-cell assembler is 1.0 ± 0.1 g cm^{-3} (Table S2, Supporting Information). HRTEM analysis (Figure 3c) shows sulfur nanoparticles of 2 to 3 nm size adhering to the CNTs, which is in accordance with the X-ray diffraction (XRD, Figure S5b, Supporting Information) and Raman data (Figure S5c, Supporting Information).

The galvanostatic charge/discharge curves (Figure 3d) and cyclic voltammograms (CVs, Figure S6a, Supporting Information) of the S/CNT-UGF cathode (45 wt% sulfur content) measured with respect to a lithium metal foil as anode (Li-foil||S/CNT-UGF) show characteristics of elemental sulfur reversibly reacting with lithium during charge/discharge.[12,14] The small voltage difference of 0.3 V for the discharge plateaus between 0.5 and 8 C suggests suppressed polarization. The electrochemical impedance spectroscopy (EIS) measurements performed on the S/CNT-UGF cathode show that the Warburg impedance is negligible (Figure S6b, Supporting Information) and the charge transfer resistances are 37 and 27 Ω, respectively, before (Figure S6c, Supporting Information) and after (Figure S6d, Supporting Information) cycling, which are much lower than that of the traditional cathode (Figure S6e, Supporting Information). These results indicate an excellent rate capability of the S/CNT-UGF cathode as shown in Figure S6f of the Supporting Information. Apart from the impressive high-rate capability, the S/CNT-UGF cathode (43 wt% sulfur content) delivered a specific capacity (based on the mass of sulfur) of 1090 mA h g^{-1} in the 1st cycle and 818 mA h g^{-1} in the 400th cycle at 0.5 C, corresponding to an average decay rate of 0.063% per cycle. This result indicates a suppression of soluble polysulfide shuttling, which has been confirmed by charging/discharging the S/CNT-UGF (Figure S7b, Supporting Information) and the cathode made of a sulfur/graphene composite coated on an aluminum foil (Figure S7a, Supporting Information) in glass cells. The UV–vis spectra (Figure S7c, Supporting Information) of the electrolytes show that the concentration of the soluble polysulfide released from the S/CNT-UGF cathode is 1/6 of that released from the sulfur/graphene composite coated on the aluminum foil. The suppressed shuttle effect may be ascribed to

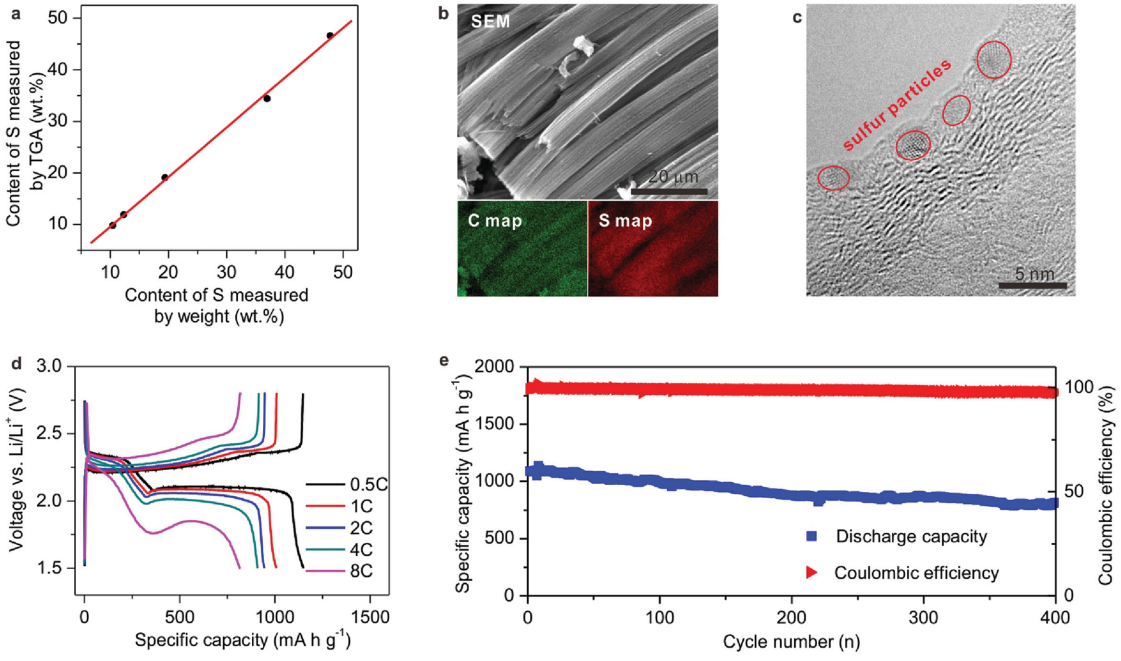

Figure 3. a) The sulfur content of the S/CNT-UGF as measured by the weight difference of the CNT-UGF hybrid before and after sulfur loading was in the range of 11–47 wt% and this was verified by TGA. We obtained a straight line with a fitted slope of 0.9975 when plotting the mass ratio of sulfur measured by weighing against that measured by TGA. b) SEM image (top) and the carbon (bottom left) and sulfur (bottom right) EDX elemental maps of the S/CNT-UGF composite, showing a homogeneous sulfur distribution in the CNT bundles. c) HRTEM image of the nanometer sulfur particles marked by red circles. d) Galvanostatic charge/discharge profiles of the S/CNT-UGF cathode (45 wt% sulfur content) measured with respect to a Li foil at different cycling rates. The lower discharge plateaus dropped from 2.10 V for 0.5 C to 2.09, 2.06, 2.01, and 1.80 V, respectively, when gradually increasing the discharge rate to 1, 2, 4, and 8 C. e) Cycling performance of the S/CNT-UGF cathode (43 wt% sulfur content) measured at 0.5 C for 400 cycles. The average decay rate of the specific capacity is 0.063% per cycle, and the Coulombic efficiencies at the 3rd, 200th, and 400th cycle are 99.9%, 99.0%, and 97.5%, respectively.

ADVANCED MATERIALS
www.advmat.de

www.MaterialsViews.com

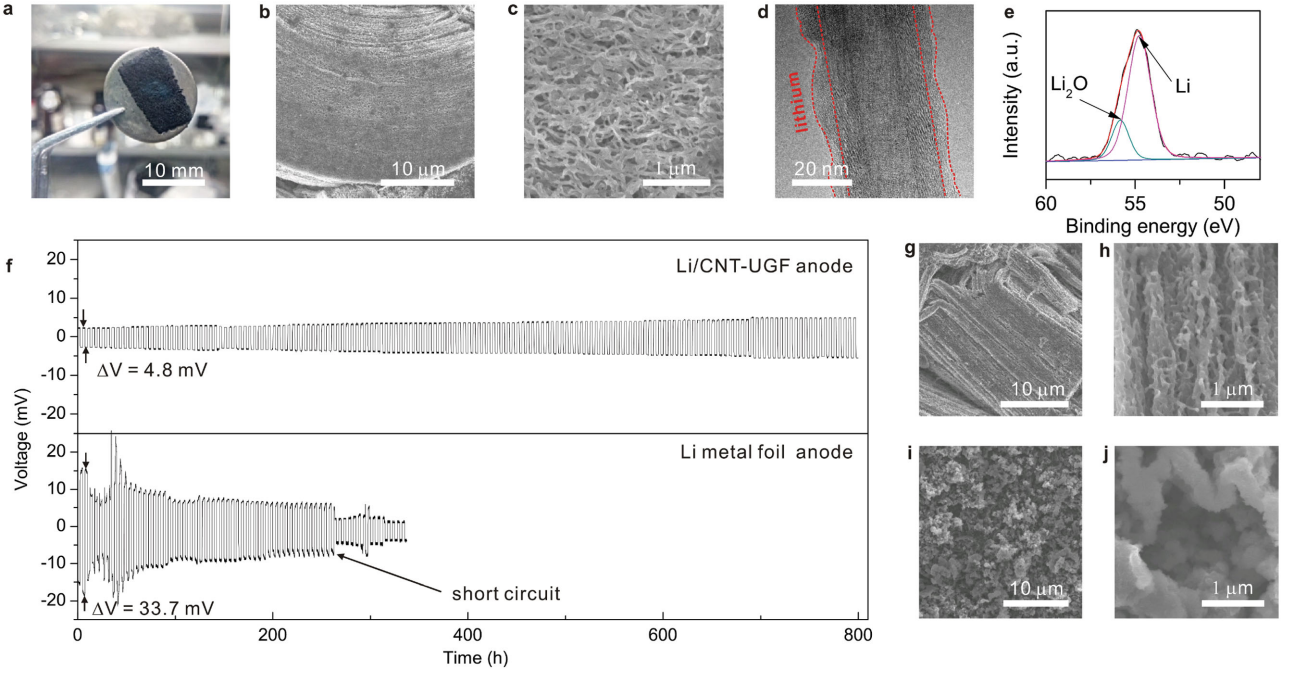

Figure 4. a) Photograph of CNT-UGF after electroplating with lithium at a current density of 0.5 mA cm^{-2} for 20 h. b,c) SEM images of CNT-UGF after electroplating with lithium. d) TEM image of a single CNT with a lithium coating. e) XPS spectrum of a Li/CNT-UGF anode showing the Li 1s peak. f) Voltage profiles of lithium metal plating/stripping at 0.25 mA cm^{-2} in a symmetric Li||Li cell with (upper panel) and without (lower panel) a CNT-UGF current collector. g,h) SEM images of a Li/CNT-UGF anode after 800 h plating/stripping. i,j) SEM images of a lithium metal foil after 350 h plating/stripping.

the "narrow" and "long" channel between the CNTs, in which the generated polysulfides need a longer diffusion time before escaping into the electrolyte, so that a better "trapping" effect is realized.

We electroplated lithium metal on CNT-UGF in a two-electrode cell (see Experimental Section of Supporting Information) at a constant current density of 0.5 mA cm^{-2} for 20 h to reach an areal capacity of 10 mAh cm^{-2}.[36] A photograph of the Li/CNT-UGF anode shows the color of black carbon (**Figure 4**a) and a low magnification SEM image (Figure 4b and Figure S8a, Supporting Information) show CNT bundles that are similar to those in the CNT-UGF without lithium plating (Figure 1b,f). Higher magnification SEM (Figure 4c) and TEM images (Figure 4d and Figure S9a, Supporting Information) show the coexistence of Li and SEI on the CNTs, which is also confirmed by the Fourier transform infrared spectrum (FT-IR, Figure S9b, Supporting Information) and the X-ray photoelectron spectra (XPS, Figure 4e and Figure S10a, Supporting Information). These results indicate that the lithium is plated on the surface of the CNT with the structure features of the CNT-UGF preserved. Upon elevating the current density to 2, 10 and finally to 20 mA cm^{-2}, the Li/CNT-UGF electrodes show almost unchanged morphology and width of the Li-coated CNTs after reaching the areal capacity of 10 mAh cm^{-2} (Figure S11, Supporting Information). This result proves the effect of 3D carbon network in preventing the lithium dendrite formation. The Li/CNT-UGF could accommodate up to 36 wt% Li with a compressed mass density of 0.8 ± 0.1 g cm^{-3} (Table S3, Supporting Information) without the formation of micrometer-size Li metal grains (Figure 4a). Given such a Li content, the theoretical capacity of Li/CNT-UGF anode is 1390 mAh g^{-1} (based on the total mass of the anode), which is three times higher than the commercial graphite anode (372 mAh g^{-1}). Nevertheless, if we increase the areal capacity (e.g., to 15 mAh cm^{-2}) by extending the electroplating time or enlarging the current density, lithium metal will be visible on top of the CNT-UGF with the naked eye and SEM (Figure S10b,c, Supporting Information).

We studied the electrochemical property of lithium plating/stripping and the cycling stability of the Li/CNT-UGF anode by galvanostatic charge/discharge voltage profiles (see Experimental Section of Supporting Information).[36] During Li plating/stripping at a constant current density of 0.25 mA cm^{-2} with respect to the geometric area of the working electrodes, the Li/CNT-UGF shows excellent stability with negligible voltage fluctuation during cycling while the lithium foil exhibits random voltage oscillations (Figure 4f). The voltage hysteresis that is calculated by the difference between the voltage of lithium plating and stripping in each cycle is mainly determined by the current density, interfacial properties, and charge transfer rate.[25,26] This therefore indicates the polarization of the lithium plating/stripping, the stability of the lithium/electrolyte interface, and short circuiting as a result of lithium dendrite growth. The Li/CNT-UGF shows a voltage hysteresis of 4.8 mV in the initial cycles, approximately one seventh of that of a lithium foil. Although the voltage hysteresis of Li/CNT-UGF increases gradually during cycling, which is ascribable to the built-up of the SEI layer (Figure S9a, Supporting Information),[25] it is still around 10 mV after 800 h of cycling without any indication of an abrupt change if we would

continue running the cell. We have also measured the EIS of the Li‖Li and Li‖Li/CNT-UGF symmetric cells before and after 100 Li plating/stripping cycles at 0.25 mA cm^{-2} (Figure S12, Supporting Information). The Li‖Li/CNT-UGF cell shows a lower charge transfer resistances both before and after cycling comparing to the Li‖Licell. And its resistance values increases 18% upon cycling, which is in accordance with the change of the voltage hysteresis as shown in Figure 4f. The stable increment of the voltage hysteresis of the Li/CNT-UGF compared to the irregular fluctuation of that of the lithium foil indicates a more stable lithium/electrolyte interface when using CNT-UGF as the current collector. This is confirmed by the SEM images of the electrodes after cycling which indicate that the morphology of the Li/CNT-UGF is almost unchanged (Figure 4g,h and Figure S8a,b, Supporting Information) although dendrites are clearly visible on the lithium foil (Figure 4i,j and Figure S8c, Supporting Information). The voltage hysteresis of the lithium foil drops abruptly to around 10 mV after 260 h of cycling due to the dendrite induced short circuit, but such a drop is not observed for the Li/CNT-UGF (Figure 4f).

To demonstrate the function of CNT-UGF as a current collector for both the cathode and anode in a Li–S battery, we assembled a S/CNT-UGF cathode (47 wt% sulfur content, 2.6 g cm^{-2} areal loading density of sulfur) and a Li/CNT-UGF anode (20 wt% lithium content) in a full cell. The Li/CNT-UGF‖S/CNT-UGF cell delivered specific capacities of 1150, 1050, 1000, 950, 910, and 860 mAh g^{-1}, respectively, at 0.5, 1, 2, 3, 6, and 12 C with respect to the mass of sulfur (**Figure 5**a,b). The specific power of the Li/CNT-UGF‖S/CNT-UGF cell calculated based on the mass of the S/CNT-UGF cathode (the lithium mass is excessive in the anode) reaches 8680 W kg^{-1} with a specific energy of 720 W h kg^{-1} (at 12 C, Figure 5c). The same electrode can also deliver a maximum specific energy of 1130 W h kg^{-1} with a specific power of 560 W kg^{-1} (at 0.5 C). The mass density of the S/CNT-UGF cathode is 1.0 ± 0.1 g cm^{-3}, which is obtained by measuring the weight and dimensions of the compressed electrode (Table S2, Supporting Information), and this yields a volumetric power density of 8680 W L^{-1} at an energy density of 720 W h L^{-1} (at 12 C), and a volumetric power density of 560 W L^{-1} at an energy density of 1130 W h L^{-1} (at 0.5 C) with respect to the volume of the cathode. The power and energy output of the S/CNT-UGF cathode is considerably higher than that in most previous reports (Figure 5c and Table S4, Supporting Information).[6,9–12,16,18,20,37] The cycling life of the Li/CNT-UGF‖S/CNT-UGF cell was measured at 2 C, which delivers a specific capacity with respect to the mass of sulfur of 1007 and

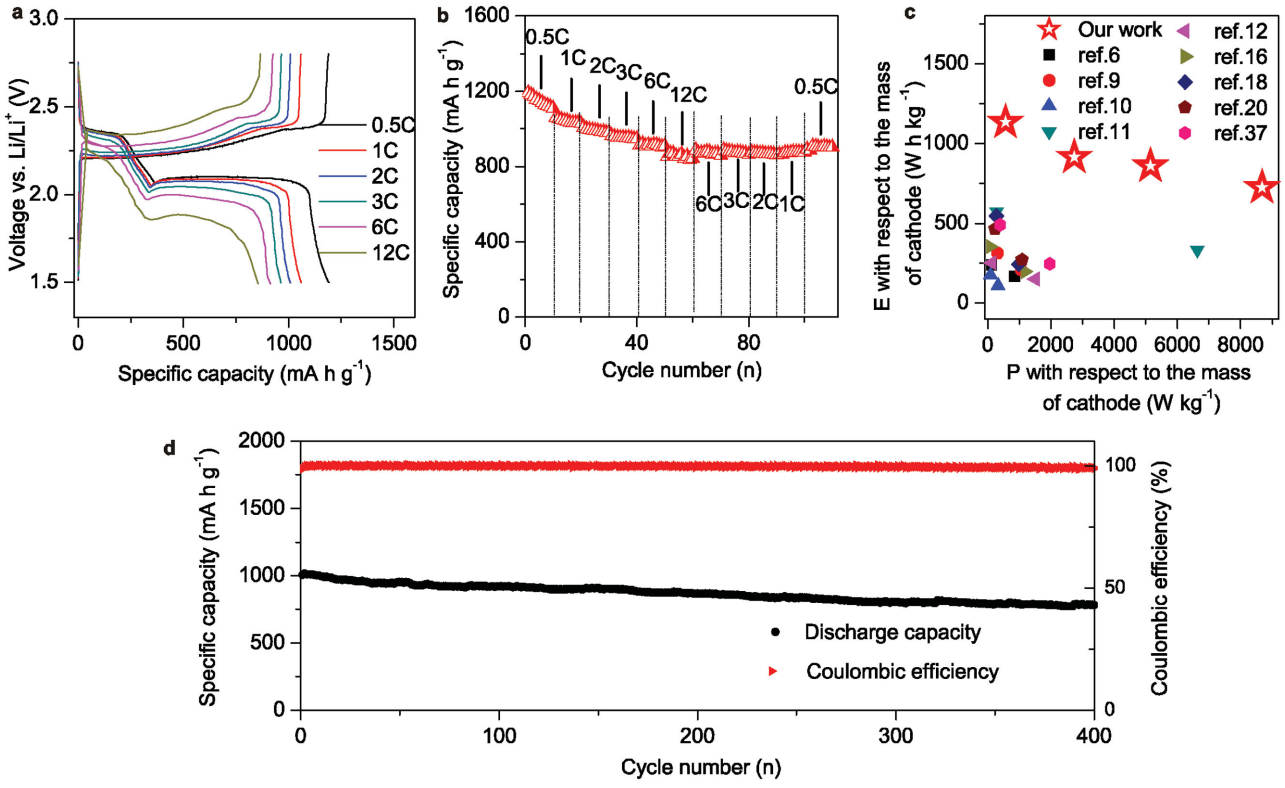

Figure 5. a) Galvanostatic charge/discharge profiles of the Li–S cell under different C rates. The lower discharge plateau decreases from 2.10 V at 0.5 C to 1.87 V at 12 C. b) Rate capabilities of the Li–S cell with a sulfur content of 47 wt% in S/CNT-UGF cathode and a Li content of 20 wt% in the Li/CNT-UGF anode tested at 0.5, 1, 2, 3, 6, and 12 C. The specific capacity at 12 C is 73.7% of that at a rate of 0.5 C. c) Calculated Ragone plot based on the electrochemical data in b with respect to the mass of the S/CNT-UGF cathode. Some previous results of high-end Li–S batteries are also shown for reference. The specific power and energy reported in references were calculated with respect to the mass of the whole cathode containing the composite, binder, carbon black and aluminum current collector. d) Cycling performance of the Li–S battery with a S/CNT-UGF cathode (47 wt% sulfur content) and a Li/CNT-UGF anode (20 wt% Li content) measured at 2 C for 400 cycles. The average decay rate of the specific capacity is 0.057% per cycle, and the Coulombic efficiencies at the 400th cycle is 99.8%.

776 mAh g^{-1} at the 1st and the 400th cycle respectively. The average decay rate of the specific capacity is 0.057% per cycle, and the Coulombic efficiency at the 400th cycle is 99.8%.

A current collector needs to allow a uniform distribution of electrode materials, be highly conductive and lightweight. The CNT-UGF has a large porosity and a low mass density (SSA of 252 m^2 g^{-1}, pore volume of 1.08 cm^3 g^{-1} and density of 12.4 mg cm^{-3}, Figure 1g,j,k). And the excellent wettability of sulfur on carbon ensures a uniform distribution of sulfur nanoparticles with a mass content of 47 wt% directly adhering to the CNTs without using any binder or carbon black (Figure 3b,c). The sulfur mass content of 47 wt% is comparable with, or higher than that on conventional current collectors made of aluminum foil (Table S4, Supporting Information). On the other hand, the CNT-UGF current collector has a freestanding interconnected network composed of sp^2-hybridized carbon nanostructures that are covalently connected by carbon–carbon bonds, allowing a ready flow of electrons within the overall electrode, and therefore affording a remarkable rate capability (Figure 5b,c).

We suggest that the remarkable specific power of the S/CNT-UGF cathode is due to the structure of the CNT-UGF current collector. This is verified by comparing the discharge capacities at the upper and lower plateaus of the galvanostatic charge/discharge profiles in Figure 5a. When discharging, elemental sulfur is first transformed into highly soluble long-chain polysulfides ($S_8 \leftrightarrow Li_2S_4$) in the potential range of 2.4 – 2.1 V (upper plateau of the black curve in Figure 5a). Then the long-chain polysulfides undergo a nucleation reaction and are converted to nonsoluble Li_2S_2 and Li_2S ($Li_2S_4 \leftrightarrow Li_2S$) in the potential range of 2.1 – 1.5 V (lower plateau of the black curve in Figure 5a).[1] The lower plateau contributes a theoretical capacity of 1256 mA h g^{-1}, three times that of the upper plateau. However, its slower reaction kinetics result in a greater decrease of the lower-plateau capacity which accounts for the low rate capability of the cell (**Figure 6**a).[38] Nevertheless, when CNT-UGF is used, the lower-plateau capacity (550 mAh g^{-1}) is still 1.8 times that of the upper-plateau capacity (310 mAh g^{-1}) at 12 C (Figure 6a), indicating that the conversion of soluble Li_2S_4 to nonsoluble Li_2S contributes almost two thirds of the discharge capacity for high-rate cycling. The improved reaction kinetics in the lower plateau are ascribable to the CNT-UGF current collector design in which the charges generated at the interface of the electrolyte and sulfur/polysulfide nanoparticles can transfer to the 3D interconnected current collector without the scattering produced by interparticle boundaries (Figures 1 and 2). In addition, we note that the hystereses of the charge/discharge curves are smaller and the specific capacities are larger for the Li/CNT-UGF‖S/CNT-UGF cell comparing to that of the Li-foil‖S/CNT-UGF cell at different C-rates (Figure S13, Supporting Information). A smaller hysteresis and a larger specific capacity indicate an improved rate capability of the Li–S cell with the Li/CNT-UGF anode than of the cell with the Li-foil anode, which is due to the CNT-UGF current collector with lithium being confined in highly conductive 3D network showing a significant kinetic advantage over bare lithium foil, especially at higher charge/discharge rates.

The Li/CNT-UGF‖S/CNT-UGF cell can deliver a remarkable high-rate capacity of 860 mA h g^{-1} (with respect to the mass of sulfur) at 12 C (Figure 5a,b), corresponding to a maximum specific power of 8680 W kg^{-1} at a specific energy of 720 W h kg^{-1} with respect to the mass of the S/CNT-UGF cathode (Figure 5c). The weight of a cathode for a typical Li–S cell is around 33.3 wt% of the whole battery. Thus a Li/CNT-UGF‖S/CNT-UGF cell would be able to work at a high specific power of 2890 W kg^{-1} with a specific energy of 240 W h kg^{-1} (12 C). Alternatively the cell could produce output in a high energy mode at a specific energy of 376 W h kg^{-1} with a specific power of 187 W kg^{-1} (0.5 C). High specific power is typically achieved at the expense of reduced specific energy, and vice versa. For example, a commercial Li-ion cell for electric vehicles can deliver a specific energy of 220 W h kg^{-1} with a specific power of less than 200 W kg^{-1}, however the specific energy drops to less than 10 W h kg^{-1} when working at a specific power of 1000 W kg^{-1}.[39] A Li–S battery with a S/CNT-UGF cathode allows the battery to be charged in approximately 5 min to an energy loading comparable to that of a Li-ion battery charged for 1 h.

In the Li/CNT-UGF anode, the relatively stable electrochemical performance is the result of the negligible morphology change after 800 h of lithium plating/stripping where the features of the CNT bundles are clearly visible in the SEM images (Figure 4g,h and Figure S8b, Supporting Information). Previous studies have identified the electrode current density as the most critical factor that triggers dendrite nucleation. Rosso

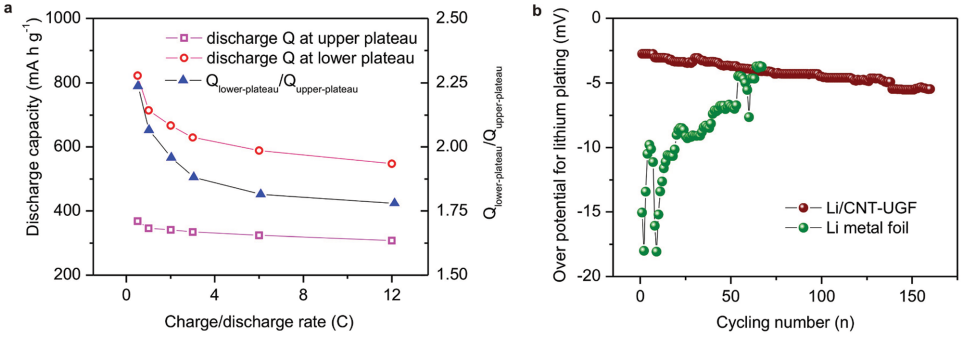

Figure 6. a) Specific capacity in the upper and lower plateaus (left axis) and their ratios (right axis) for the discharge curves in Figure 5a measured at different C-rates. The upper-plateau capacity of the S/CNT-UGF at 12 C retains 83.7% of that at 0.5 C, and the lower-plateau capacity at 12 C is 66.4% of that at 0.5 C. b) Over-potential of the Li/CNT-UGF and lithium metal foil electrodes for electroplating lithium at a current density of 0.25 mA cm^{-2} with respect to the geometric area of the working electrodes. The over-potential value in each cycle was obtained from the voltage profiles in Figure 4f.

et al. observed that the dendritic growth of lithium metal starts at a time (τ) that follows a power law as a function of the current density, very close to Sand's law[28,29]

$$\tau \sim \pi D\left(\frac{eC_0}{2J}\right)^2\left(\frac{\mu_a+\mu_c}{\mu_a}\right)^2 \quad (1)$$

where D is the ambipolar diffusion coefficient, e is the electronic charge, C_0 is the electrolyte concentration in the bulk solution, μ_a and μ_c are the anionic and cationic mobilities, and J is the practical current density at the anode surface. Therefore, a smaller current density at the electrode surface results in a larger τ that delays the nucleation of dendrites. Chazalviel suggests that the dendrite front grows at a velocity of $v = -\mu_a E_0$ where μ_a is the mobility of anions (Li^+) and the E_0 is the electric field in the neutral region which is determined by $J = eC_0(\mu_a + \mu_c)E_0$.[29] Therefore, the practical current density J determines both the nucleation and growth of the dendrites. Figure 6b shows an initial overpotential for the Li/CNT-UGF anode ($\eta_{CNT\text{-}UGF} = -2.7$ mV) that is around one seventh of that of lithium metal foil ($\eta_{CNT\text{-}UGF} = -18$ mV), and at low current densities, the over-potential η is proportional to the practical current density J.[40] Therefore, one can expect that for dendrite growth on Li/CNT-UGF the values of τ and v are, respectively, 50 and 1/7 times those for the growth of dendrites on the lithium metal foil. On the other hand, the large surface area of the UGF-CNT leads to ultrathin Li film with thickness of 2 nm on the CNTs (Figure 4d), which will be unable to generate significant volumes of Li dendrites.[41,42] Therefore, one can conclude that the dendrite formation on Li/CNT-UGF is greatly suppressed owing to the larger electrochemically active surface formed by the CNT-UGF current collector.

We have demonstrated a 3D current collector composed of hundreds of micrometer-long CNTs and UGF that are connected by covalent carbon–carbon bonds for both the sulfur cathode and the lithium anode. A Li–S battery composed of an S/CNT-UGF cathode and a Li/CNT-UGF anode delivered a remarkable high-rate capacity of 860 mAh g^{-1} with respect to the mass of sulfur at 12 C and excellent cycling stability for 400 cycles with 0.057% capacity decay per cycle. And the Li/CNT-UGF anode can run for more than 800 h without dendrite formation or short circuiting. These results are due to the CNT-UGF structure in which a covalently bonded carbon network allows a ready flow of electrons within the overall sulfur cathode without scattering at nanostructure boundaries, and the large electroactive area between lithium and the electrolyte suppresses the practical current density and thus the dendrite growth. With the scale-up potential of the CNT-UGF, one can be optimistic about its commercial possibilities. For example, a large Li–S pouch cell may be prepared by stacking the S/CNT-UGF cathode sheet and the Li/CNT-UGF anode sheet with a separator in between. The realization of such a Li–S cell requires more efforts regarding the electrolyte content, cell sealing, electrode tab welding, cathode and anode mass matching, and so on. Moreover, in view of the versatility of the synthesis methods, our strategy may be extended to design other carbon nanostructures for use in batteries and supercapacitors, making our work a valuable contribution to the field of electrical energy storage in general.

Supporting Information

Supporting Information is available from the Wiley Online Library or from the author.

Acknowledgements

S.J. and S.X. contributed equally to this work. The authors appreciate funding support from the Natural Science Foundation of China (21373197), support from the 100 Talents Program of the Chinese Academy of Sciences, USTC Startup, the Fundamental Research Funds for the Central Universities (WK2060140018 and WK 3430000003), and *i*ChEM. S.X. thanks National Natural Science Foundation of China for support (Grant No. 21403050), and the Fundamental Research Funds for the Central Universities (Grant Nos. J2014HGBZ0126 and 2014HGQC0015). L.N.C. and J.L.L. thanks National Natural Science Foundation of China for support the NSFC (51402283). X.H.K. thanks the Anhui Provincial Natural Science Foundation for support (Grant No. 1508085QE103). R.S.R. was supported by IBS-R019-D1. The authors thank Prof. L. Nazar for valuable suggestions.

Received: May 22, 2016
Revised: July 12, 2016
Published online: September 8, 2016

[1] P. G. Bruce, S. A. Freunberger, L. J. Hardwick, J. M. Tarascon, *Nat. Mater.* **2012**, *11*, 19.
[2] A. Manthiram, Y. Fu, Y. S. Su, *Acc. Chem. Res.* **2013**, *46*, 1125.
[3] S. Evers, L. F. Nazar, *Acc. Chem. Res.* **2013**, *46*, 1135.
[4] H. Kim, G. Jeong, Y. U. Kim, J. H. Kim, C. P. Park, H. J. Sohn, *Chem. Soc. Rev.* **2013**, *42*, 9011.
[5] W. Xu, J. Wang, F. Ding, X. Chen, E. Nasybulin, Y. Zhang, J. G. Zhang, *Energy Environ. Sci.* **2014**, *7*, 513.
[6] H. Kim, J. Lee, H. Ahn, O. Kim, J. M. Park, *Nat. Commun.* **2015**, *6*, 7278.
[7] J. Wang, Y. S. He, J. Yang, *Adv. Mater.* **2015**, *27*, 569.
[8] X. Ji, L. F. Nazar, *J. Mater. Chem.* **2010**, *20*, 9821.
[9] C. Tang, Q. Zhang, M. Q. Zhao, J. Q. Huang, X. B. Cheng, G. L. Tian, H. J. Peng, F. Wei, *Adv. Mater.* **2014**, *26*, 6100.
[10] Z. Xiao, Z. Yang, L. Wang, H. Nie, M. Zhong, Q. Lai, X. Xu, L. Zhang, S. Huang, *Adv. Mater.* **2015**, *27*, 2891.
[11] Y. Zhou, C. Zhou, Q. Li, C. Yan, B. Han, K. Xia, Q. Gao, J. Wu, *Adv. Mater.* **2015**, *27*, 3840.
[12] M. Q. Zhao, Q. Zhang, J. Q. Huang, G. L. Tian, J. Q. Nie, H. J. Peng, F. Wei, *Nat. Commun.* **2014**, *5*, 3410.
[13] X. Ji, S. Evers, R. Black, L. F. Nazar, *Nat. Commun.* **2011**, *2*, 325.
[14] Y. S. Su, A. Manthiram, *Nat. Commun.* **2012**, *3*, 1166.
[15] G. Zhou, D. W. Wang, X. Shan, S. Pei, F. Li, H. M. Cheng, *Adv. Mater.* **2015**, *27*, 641.
[16] M. K. Song, Y. Zhang, E. J. Cairns, *Nano Lett.* **2013**, *13*, 5891.
[17] X. Ji, K. T. Lee, L. F. Nazar, *Nat. Mater.* **2009**, *8*, 500.
[18] M. Q. Zhao, H. J. Peng, G. L. Tian, Q. Zhang, J. Q. Huang, X. B. Cheng, C. Tang, F. Wei, *Adv. Mater.* **2014**, *26*, 7051.
[19] S. Xin, L. Gu, N. H. Zhao, Y. X. Yin, L. J. Zhou, Y. G. Guo, L. J. Wan, *J. Am. Chem. Soc.* **2012**, *134*, 18510.
[20] Z. Wang, Y. Dong, H. Li, Z. Zhao, H. B. Wu, C. Hao, S. Liu, J. Qiu, X. W. Lou, *Nat. Commun.* **2014**, *5*, 5002.
[21] M. S. Whittingham, *Proc. IEEE* **2012**, *100*, 1518.

[22] M. S. Whittingham, *Science* **1976**, *192*, 1126.
[23] J. Qian, W. A. Henderson, W. Xu, P. Bhattachrya, M. Engelhard, O. Borodin, J. G. Zhang, *Nat. Commun.* **2015**, *6*, 6362.
[24] M. S. Park, S. B. Ma, D. J. Lee, D. Im, S. G. Doo, O. Yamamoto, *Sci. Rep.* **2014**, *4*, 3815.
[25] G. Zheng, S. K. Lee, Z. Liang, H. W. Lee, K. Yan, H. Yao, H. Wang, W. Li, S. Chu, Y. Cui, *Nat. Nano* **2014**, *9*, 618.
[26] K. Yan, H. W. Lee, T. Gao, G. Zheng, H. Yao, H. Wang, Z. Lu, Y. Zhou, Z. Liang, Z. Liu, S. Chu, Y. Cui, *Nano Lett.* **2014**, *14*, 6016.
[27] S. T. Myung, Y. Hitoshi, Y. K. Sun, *J. Mater. Chem.* **2011**, *21*, 9891.
[28] M. Rosso, T. Gobron, C. Brissot, J. N. Chazalviel, S. Lascaud, *J. Power Sources* **2011**, *97*, 804.
[29] J. N. Chazalviel, *Phys. Rev. A.* **1990**, *42*, 7355.
[30] H. Ji, L. Zhang, M. T. Peter, H. Li, S. Chen, L. Shi, R. Piner, R. S. Ruoff, *Nano Lett.* **2012**, *12*, 2446.
[31] J. Ji, H. Ji, L. L. Zhang, X. Zhao, X. Bai, X. Fan, F. Zhang, R. S. Ruoff, *Adv. Mater.* **2013**, *25*, 4673.
[32] Z. Chen, W. Ren, L. Gao, B. Liu, S. Pei, H. M. Cheng, *Nat. Mater.* **2011**, *10*, 424.
[33] W. D. Zhang, Y. Wen, W. C. Tjiu, G. Q. Xu, L. M. Gan, *Appl. Phys. A* **2002**, *74*, 419.
[34] S. Fan, M. G. Chapline, N. R. Franklin, T. W. Tombler, A. M. Cassell, H. Dai, *Science* **1999**, *283*, 512.
[35] C. L. Pint, N. T. Alvarez, R. H. Hauge, *Nano Res.* **2010**, *2*, 526.
[36] C. P. Yang, Y. X. Yin, S. F. Zhang, N. W. Li, Y. G. Guo, *Nat. Commun.* **2015**, *6*, 8058.
[37] C. Huang, J. Xiao, Y. Shao, J. Zheng, W. D. Bennett, D. Lu, L. V. Saraf, M. Engelhard, L. Ji, J. Zhang, X. Li, G. L. Graff, J. Liu, *Nat. Commun.* **2014**, *5*, 3015.
[38] Y. S. Su, Y. Fu, B. Guo, S. Dai, A. Manthiram, *Chem. Eur. J.* **2013**, *19*, 8621.
[39] P. Simon, Y. Gogotsi, *Nat. Mater.* **2008**, *7*, 845.
[40] A. J. Bard, L. R. Faulkner, *Electrochemical Methods: Fundamentals and Applications*, 2nd ed., John Wiley & Sons, New York, **2000**.
[41] R. Mukherjee, A. V. Thomas, D. Datta, E. Singh, J. Li, O. Eksik, V. B. Shenoy, N. Koratkar, *Nat. Commun.* **2014**, *5*, 3710.
[42] K. J. Harry, D. T. Hallinan, D. Y. Parkinson, A. A. MacDowell, N. P. Balsara, *Nat. Mater.* **2014**, *13*, 69.